Crustal Imaging with Noisy Teleseismic Receiver Functions Using Sparse Radon Transforms

Ziqi Zhang*1 and Tolulope Olugboji1,2,3

ABSTRACT

The receiver function (RF) is a widely used crustal imaging technique. In principle, it assumes relatively noise-free traces that can be used to target receiver-side structures following source deconvolution. In practice, however, mode conversions and reflections may be severely degraded by noisy conditions, hampering robust estimation of crustal parameters. In this study, we use a sparsity-promoting Radon transform to decompose the observed RF traces into their wavefield contributions, that is, direct conversions, multiples, and incoherent noise. By applying a crustal mask on the Radon-transformed RF, we obtain noise-free RF traces with only Moho conversions and reflections. We demonstrate, using a synthetic experiment and a real-data example from the Sierra Nevada, that our approach can effectively denoise the RFs and extract the underlying Moho signals. This greatly improves the robustness of crustal structure recovery as exemplified by subsequent $H-\kappa$ stacking. We further demonstrate, using a station sitting on loose sediments in the Upper Mississippi embayment, that a combination of our approach and frequency-domain filtering can significantly improve crustal imaging in reverberant settings. In the presence of complex crustal structures, for example, dipping Moho, intracrustal layers, and crustal anisotropy, we recommend caution when applying our proposed approach due to the difficulty of interpreting a possibly more complicated Radon image. We expect that our technique will enable high-resolution crustal imaging and inspire more applications of Radon transforms in seismic signal processing.

KEY POINTS

- Sparse Radon transform is used to denoise the Ps-RF and extract Moho-related phases.
- Synthetic and data examples show that our approach can drastically reduce the ambiguity of $H \kappa$ stacking.
- Our approach can be coupled with resonance filtering to improve crustal imaging in reverberant settings.

Supplemental Material

INTRODUCTION

The receiver function (RF) is a powerful seismic imaging technique for constraining crustal structure in various tectonic settings, for example, orogenic belts (Parker et al., 2013; Yang et al., 2017), cratons (Thompson et al., 2010; Yuan, 2015; Xia et al., 2017; Krueger et al., 2021), volcanoes (Leahy et al., 2010; Rychert et al., 2013; Chen et al., 2020), oceans (Olugboji et al., 2016; Rychert et al., 2018; Kim et al., 2021), and even on other planets (Lognonné et al., 2020; Kim et al., 2021). Two ideas that are fundamental to using the technique include source deconvolution that targets receiver-side scattering (Gurrola et al., 1995; Ligorría and Ammon, 1999; Park and Levin, 2016) and modeling of the largest amplitude bodywave conversions and reflections generated from seismic

discontinuities directly beneath the station (Langston, 1979; Zandt and Ammon, 1995; Julia *et al.*, 2000; Zhu and Kanamori, 2000; Wittlinger *et al.*, 2009; Bodin *et al.*, 2013). During the modeling stage, for example, $H - \kappa$ stacking and its various adaptations (Zhu and Kanamori, 2000; Wittlinger *et al.*, 2009; Helffrich and Thompson, 2010; Rychert and Harmon, 2016), the RF traces are assumed to be relatively noise-free, permitting robust estimation of the crustal structure, that is, crustal thickness (H) and P-to-S (compressional-to-shear) velocity ratio (V_P/V_S , or κ). In practice, however, mode conversions and reflections may be severely degraded by noisy conditions. This may render the modeling step intractable, hampering robust estimation of the crustal parameters and the subsequent interpretation of crustal composition (Zandt and Ammon, 1995; Stankiewicz *et al.*, 2002; Audet *et al.*, 2009; He *et al.*, 2013). For this reason, seismic

Cite this article as Zhang, Z., and T. Olugboji (2024). Crustal Imaging with Noisy Teleseismic Receiver Functions Using Sparse Radon Transforms, *Bull. Seismol. Soc. Am.* **114**, 1600–1612, doi: 10.1785/0120230254

© Seismological Society of America

^{1.} Department of Earth and Environmental Sciences, University of Rochester, Rochester, New York, U.S.A., https://orcid.org/0000-0003-3303-2597 (ZZ); https://orcid.org/0000-0002-2621-2752 (TO); 2. Department of Electrical and Computer Engineering, University of Rochester, Rochester, New York, U.S.A.; 3. Georgen Institute of Data Sciences, University of Rochester, Rochester, New York, U.S.A.

^{*}Corresponding author: ziqi.zhang@rochester.edu

analysts usually employ a variety of quality control procedures to select high-quality RFs either manually or in an automated manner, for example, using a combination of attributes from deconvolution, waveform features, and stacking statistics (Yang et al., 2016), or through supervised machine-learning models (Gong et al., 2022). Previous studies have also made several modifications to grid-search algorithms in an effort to improve the constraints from the low-amplitude reflections, including, but not limited to, using cluster analysis and semblance weighting (Philip Crotwell and Owens, 2005; Eaton et al., 2006), varying weighting factors for different phases (Vanacore et al., 2013), and performing moveout corrections preceding the grid search (Rivadeneyra-Vera et al., 2019). In addition, several denoising frameworks have been proposed to aid with the interpretation of noisy RF data, including transform-based methods (Chen et al., 2019, 2022; Dalai et al., 2019; Zhang et al., 2021, 2022;), rank-reduction techniques (Dokht et al., 2016; Rubio et al., 2020), and machine-learning frameworks (Dalai et al., 2021; Wang et al., 2022).

In this study, we denoise the observed RF data using a modification of a recently proposed transform-based signal processing workflow—Clean Receiver Function Imaging using SParse Radon Filter (CRISP-RF; Olugboji et al., 2023). The central idea involves applying a sparse Radon transform to effectively decompose the Ps-RF into direct conversions, multiples, and noise, based on the time-slowness moveout and phase coherence. In our implementation here, we retain the crustal multiples as well as the direct arrivals generated at the Moho. Although our approach is illustrated using the traditional $H - \kappa$ stacking technique, it may be applied prior to data modeling using other grid-search or waveform-fitting techniques (Wittlinger et al., 2009; Helffrich and Thompson, 2010; Rychert and Harmon, 2016). The improvement in crustal imaging follows from noise suppression and enhanced detection of time-slowness arrivals of converted and reflected phases that enable robust back-projection during a crustal parameter search. We start by introducing the basic principles and processing steps of CRISP-RF, and what modifications are needed to suit our goal of preserving Moho conversions and multiples. We provide synthetic experiments and a real-data example to demonstrate the effectiveness of our approach and to show that we are able to effectively denoise the RF and improve the robustness of crustal structure estimation. We demonstrate using another data example that our approach can be coupled with resonance filtering (Yu et al., 2015; Akuhara et al., 2016; Zhang and Olugboji, 2021, 2023) to improve crustal imaging in reverberant settings.

METHOD

Brief overview of RF and $H - \kappa$ stacking

P-to-S RF (*Ps*-RF) is obtained by deconvolving the parent component from the daughter component seismograms, and targets receiver-side structure with the source and path removed

(Langston, 1979; Ammon, 1991; Park and Levin, 2000; Zhong and Zhan, 2020). The choice of Z-R-T (vertical-radialtransverse) coordinate system is the most common practice; other options include L-Q-T and P-SV-SH coordinate systems (Rondenay, 2009). In this study, we use the Z-R-T coordinate system and obtain the radial RF by deconvolving the vertical component from the radial component seismograms. Assuming a simple laterally homogenous and horizontally layered model with a crust and a half-space, the Ps-RF trace should contain one direct conversion from the Moho (PmS) and two multiples (PPmS and PSmS; Fig. 1a). The $H - \kappa$ stacking method calculates the stacking amplitudes of Ps-RF traces of different slowness at the predicted arrival times of these phases using different pairs of H (crustal thickness) and κ (P-to-S velocity ratio) values, and determines the optimal result by performing a grid search (Zhu and Kanamori, 2000):

$$s(H,\kappa) = \sum_{i} \sum_{j} w_{j} G(t_{ij}) R_{j}(t), \qquad (1)$$

in which s is the stacking amplitude, t_{ij} is the predicted arrival of the ith phase (i.e., PmS, PPmS, and PSmS), G is a Gaussian smoothing window centered at time t, R_j is the jth radial Ps-RF trace, and w_j is the weighting factors for different phases. In most implementations, the direct phase is weighted higher, and the multiples are weighted lower due to their relative amplitudes (e.g., calculated from reflection and transmission coefficients in Zhang and Olugboji, 2021). Here, we use 0.4, 0.3, and -0.3 as the weighting factors for PmS, PPmS, and PSmS phases, respectively, for both synthetic and real data experiments in the following sections.

The predicted arrivals of each phase, given a single-layer model with thickness H, compressional velocity V_P , and shear velocity V_S , are given by

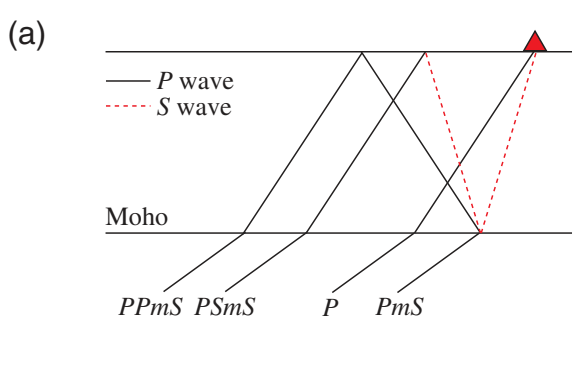
$$t_{PmS} = H\left(\sqrt{\frac{1}{V_S^2} - p^2} - \sqrt{\frac{1}{V_P^2} - p^2}\right),$$
 (2a)

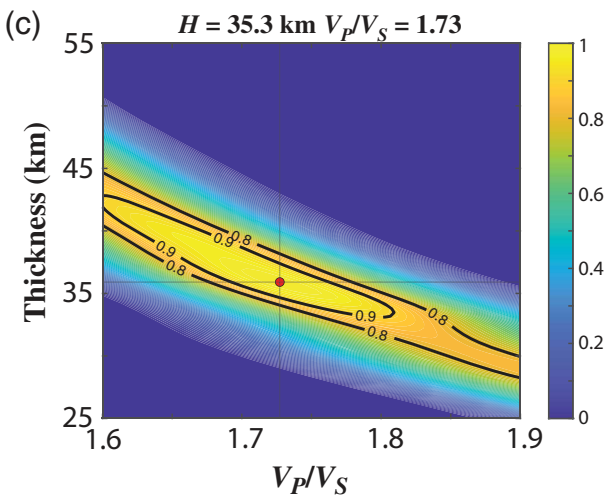
$$t_{PPmS} = H\left(\sqrt{\frac{1}{V_S^2} - p^2} + \sqrt{\frac{1}{V_P^2} - p^2}\right),$$
 (2b)

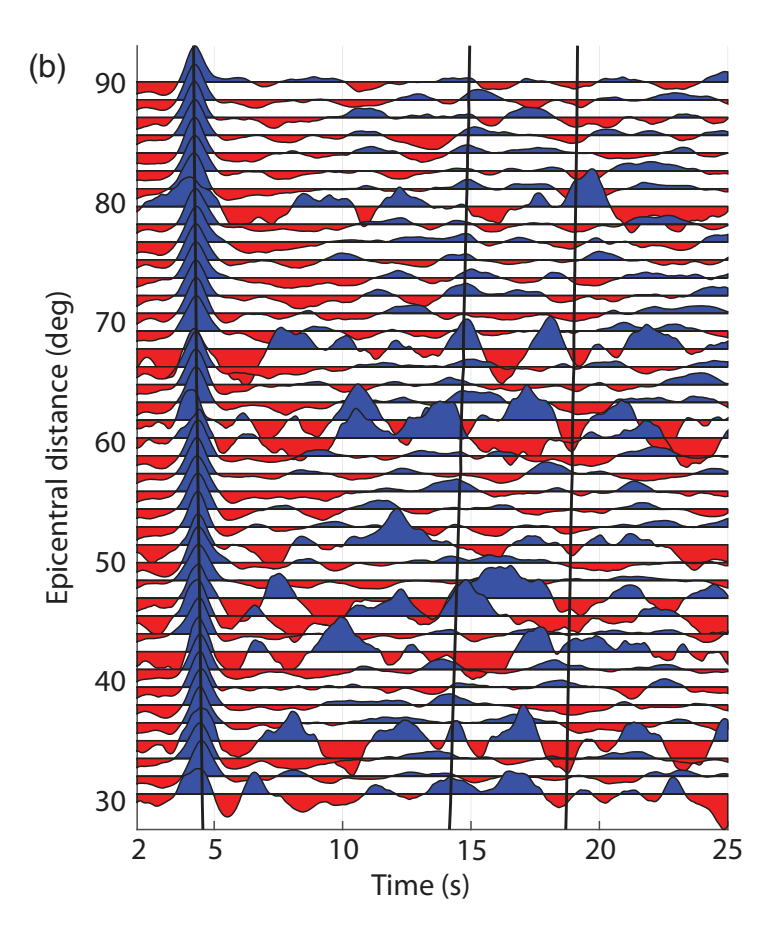
$$t_{PSmS} = 2H\left(\sqrt{\frac{1}{V_S^2} - p^2}\right),\tag{2c}$$

in which p is the slowness of the Ps-RF trace.

A crustal compressional velocity (V_P) is usually assumed in the $H - \kappa$ stacking so that the shear velocity (V_S) in equation (2) can be substituted by $V_S = \frac{V_P}{\kappa}$. This a priori assumption is not necessary for some of the adaptations of the $H - \kappa$ stacking; for







example, Rychert and Harmon (2016) used both Ps- and Sp-RF in their stacking algorithm so that crustal parameters H, V_P , and V_S can be determined without assuming its elastic properties. Other examples include Kumar and Bostock (2008), which used least-squares regression to solve for V_P and κ and Helffrich and Thompson (2010), which improved the reliability of V_P and κ estimates when events with small slownesses are not available. Nevertheless, for simplicity, we illustrate our approach using the traditional $H - \kappa$ stacking technique.

Application of CRISP-RF: Sparse Radon transform and crustal mask

CRISP-RF and sparse Radon transform. The slowness-binned *Ps*-RF stacks can be viewed as a 2D matrix with 1D representing the slowness (or epicentral distance in a 1D earth model) and the other representing the time axis. Applying the Radon transform to this matrix allows us to describe the *Ps*-RF data **d** by a sparse model set **m**:

$$\mathbf{d}(t,p) = \mathfrak{R}^{\dagger}\{\mathbf{m}(\tilde{\tau},q)\} \triangleq \sum_{i=1}^{N_q} \mathbf{m}(\tilde{\tau} = t - q_i p^2, q_i), \quad (3)$$

in which $\mathbf{d}(t,p)$ is the *Ps*-RF data in the time-slowness domain, $\mathbf{m}(\tilde{\tau},q)$ is the Radon model in the intercept-time-curvature domain (here intercept-time refers to the arrival time assuming zero slowness, and curvature refers to the extent of the moveout of the phases; Fig. 2a), and \mathfrak{R}^{\dagger} is the adjoint Radon

Figure 1. (a) Wave propagation of the direct P wave, direct P-to-S conversion at the Moho (PmS), and its multiples (PPmS and PSmS). (b) Synthetic Ps-receiver function (RF) traces of single-layer model plotted against epicentral distance. RF amplitudes are attenuated from 100% at 0 s to 10% at 12 s. Realistic noise with a signal-to-noise ratio (SNR) of 2.0 is added to all RF traces. Additional noise with an SNR of 0.5 is added to 10 randomly chosen traces. Black vertical lines indicate theoretical arrivals for PmS, PPmS, and PSmS phases, respectively. (c) $H - \kappa$ stacking of the synthetic Ps-RF shown in panel (b). The stacking image displays a stripe feature, indicating that the Ps-RF traces are dominated by the PmS phase. Black contour lines indicate 90% and 80% of the maximum stacking amplitude. For better visualization, we set all negative stacking amplitudes to zero. The color version of this figure is available only in the electronic edition.

transform. Ideally, the Radon model (**m**) should only have nonzero amplitudes at intercept-time and curvature pairs corresponding to coherent arrival phases, that is, PmS, PPmS, and PSmS in the single-layer scenario (Fig. 2b). The adjoint Radon transform \Re^{\dagger} reconstructs the Ps-RF data (**d**) by summing the amplitudes of the Radon model at all curvature (q_i) along each slowness (p).

The CRISP-RF workflow starts by applying a sparsity-promoting Radon transform that effectively decomposes the input *Ps*-RF data into direct conversions, multiple reflections, and incoherent noise (Olugboji *et al.*, 2023). Here, we demonstrate the performance of the sparsity-promoting Radon transform for noise suppression using a synthetic *Ps*-RF generated for a single-layer model with a crustal thickness of 35 km, a compressional

TABLE 1

Detailed $H - \kappa$ Stacking Results of Synthetic Experiments and Real-Data Examples

Case	Figure(s)	H _{raw} (km)	H _{filtered} (km)	H Improvement	κ_{raw}	$\kappa_{ m filtered}$	κ Improvement
Synthetic WCN HENM	Figures 1, 2, 4 Figure 6 Figure 7	35.3 ^{+7.58} 35.3 ^{+2.95} 34.0 ^{+1.14} -2.26	35.0 ^{+1.53} 35.9 ^{+1.45} 34.0 ^{+1.49}	67% 40% 38%	$1.73^{+0.079}_{-0.130} \\ 1.72^{+0.090}_{-0.087} \\ 1.85^{+0.125}_{-0.108}$	$1.75^{+0.061}_{-0.056}$ $1.69^{+0.070}_{-0.055}$ $1.85^{+0.073}_{-0.062}$	44% 29% 42%

velocity of 6.3 km/s, and a shear velocity of 3.6 km/s. To mimic the behavior of noisy realistic data, we attenuate the amplitudes (100%–10%) of the late arriving multiples (0 < t < 12 s) and then add realistic noise with a signal-to-noise ratio (SNR) of 2.0 to all the RF traces. We then add noise with a significantly lower SNR of 0.5 to 10 randomly chosen RF traces, resulting in a noisy dataset with low-amplitude multiples whose arrivals are hard to visually identify (Fig. 1b). Applying the $H - \kappa$ stacking on this Ps-RF resolves a Moho depth of 35.3 km and a P-to-S velocity ratio of 1.73 (Fig. 1c; see Table 1 for the 90% error range). The sparse Radon model calculated from the CRISP-RF workflow shows a clear separation of the three Moho-related phases, with the direct conversion being the strongest positive phase mapped into the positive curvature domain, the first multiple (PPmS) mapped into the negative curvature domain with a positive amplitude, and the second multiple (PSmS) also in the negative curvature domain but with a negative amplitude (Fig. 2).

Keeping Moho phases: crustal mask. Following the sparsity-promoting Radon transform that maps different arrivals into their corresponding intercept—time—curvature locations in the Radon image, a masking filter is applied to only retain the Moho-related phases (it is here that CRISP-RF differs from its initial goal of being used to filter out crustal multiples). The Radon-transformed and filtered RFs are effectively denoised due to the sparsity-promoting step.

The key to designing this masking filter is to determine a plausible 2D window for the intercept–time–curvature parameters that contain the phases of interest. As introduced earlier, intercept-time $(\tilde{\tau})$ refers to the phase arrival assuming zero slowness, that is, by substituting p=0 in equation (2), and the curvature (q) is the degree-two coefficient of the quadratic polynomial of the Taylor expansion of equation (2) (Ryberg and Weber, 2000; Shi *et al.*, 2020; Olugboji *et al.*, 2023):

$$t_{PmS} = \tilde{\tau}_{PmS} + q_{PmS}p^2, \tag{4a}$$

$$\tilde{\tau}_{PmS} = H\left(\frac{1}{V_S} - \frac{1}{V_P}\right) q_{PmS} \approx + \frac{H(V_P - V_S)}{2}, \quad (4b)$$

$$t_{PPmS} = \tilde{\tau}_{PPmS} + q_{PPmS} p^2, \tag{4c}$$

$$\tilde{\tau}_{PPmS} = H\left(\frac{1}{V_S} + \frac{1}{V_P}\right) q_{PPmS} \approx -\frac{H(V_P + V_S)}{2},$$
 (4d)

$$t_{PSmS} = \tilde{\tau}_{PSmS} + q_{PSmS}p^2, \tag{4e}$$

$$\tilde{\tau}_{PSmS} = 2H \frac{1}{V_S} q_{PSmS} \approx -HV_S.$$
 (4f)

The crustal masking filter for the intercept-time $(\bar{\tau})$ and curvature (q) is obtained by substituting the grid-search parameter bounds into equation 4(b), (4d), (4f), for example, for a generic crustal velocity model, H=25-55 km, $V_P=6.3$, and $V_S=3.6$ km/s. This results in three distinct line segments in the intercept-time-curvature domain, one in the positive-curvature half (PmS) and two in the negative-curvature half (PPmS) and PSmS. To account for the numeric errors along the curvature axis during the Radon transform, we further add a tolerance width to the line segments, resulting in a crustal mask that passes through both direct and multiple phases for a given range of depth (Fig. 3). The rectangular areas of PmS and PPmS phases only pass through positive amplitudes, and that of PSmS phases only passes through negative amplitudes, in accordance with the phase polarities of each respective phase.

We apply this crustal mask to the previously calculated sparse Radon model and perform the adjoint Radon transform to obtain a noise-free filtered Ps-RF, which shows significantly enhanced detections of the Moho multiples (Fig. 4a). Consequently, the $H - \kappa$ stacking shows a better constraint on the crustal structure, resolving a Moho depth of 35.0 km and a velocity ratio of 1.75 (Fig. 4b; see Table 1 for the 90% error range). This result matches the input model perfectly, and shows a 67% narrower error range on H and 44% on κ , respectively, compared to the $H - \kappa$ stacking directly on the raw synthetic Ps-RF (compare Fig. 4b with Fig. 1c; see also Table 1). The 80% error range of the $H - \kappa$ stacking on the filtered Ps-RF is from 32.43 to 37.48 km for H and from 1.670 to 1.841 for κ , which is even narrower than the 90% error range of the $H - \kappa$ stacking on the raw Ps-RF, whereas the 80% error range of the $H - \kappa$ stacking on the raw Ps-RF is outside the search range (compare Figs. 1c and 4b). This improvement largely comes from the better constraint from the multiples (PPmS and PSmS), which is made possible by the denoising effect provided by the CRISP-RF.

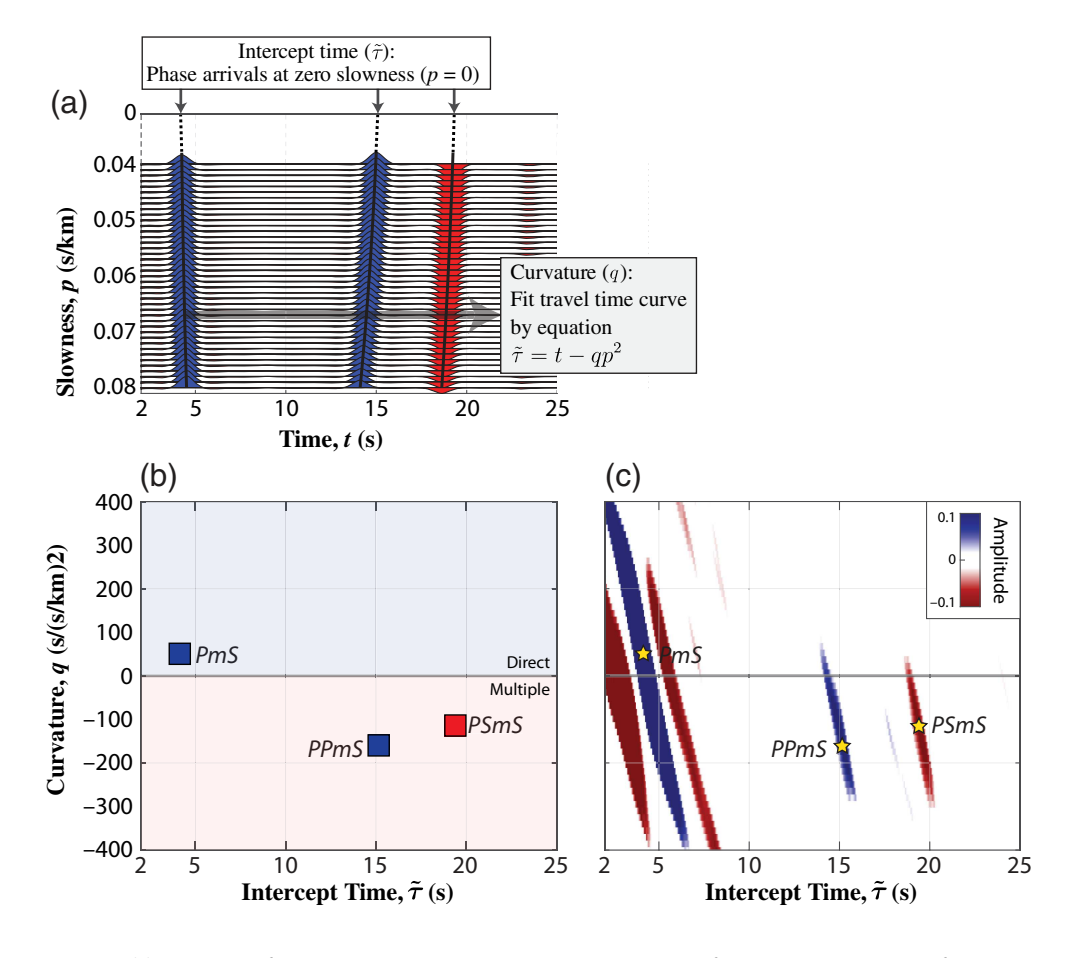


Figure 2. (a) Clean, noise-free RF image assuming a 35 km thick crust and a half-space. Intercept-time is defined as the arrival time of a phase (PmS, PPmS, or PSmS) at zero slowness (p=0); curvature is defined as the degree-two coefficient of the quadratic polynomial, as indicated in equation (4a)–(4c). (b) Synthetic Radon image of the clean RF shown in panel (a). (c) Sparse Radon model of the synthetic PS-RF shown in Figure 1b obtained from the Clean Receiver Function Imaging using SParse Radon Filter (CRISP-RF) workflow. Stars denote the theoretical ($\tilde{\tau}$,q) locations of the Moho phases calculated from equation (4b,d,f). The color version of this figure is available only in the electronic edition.

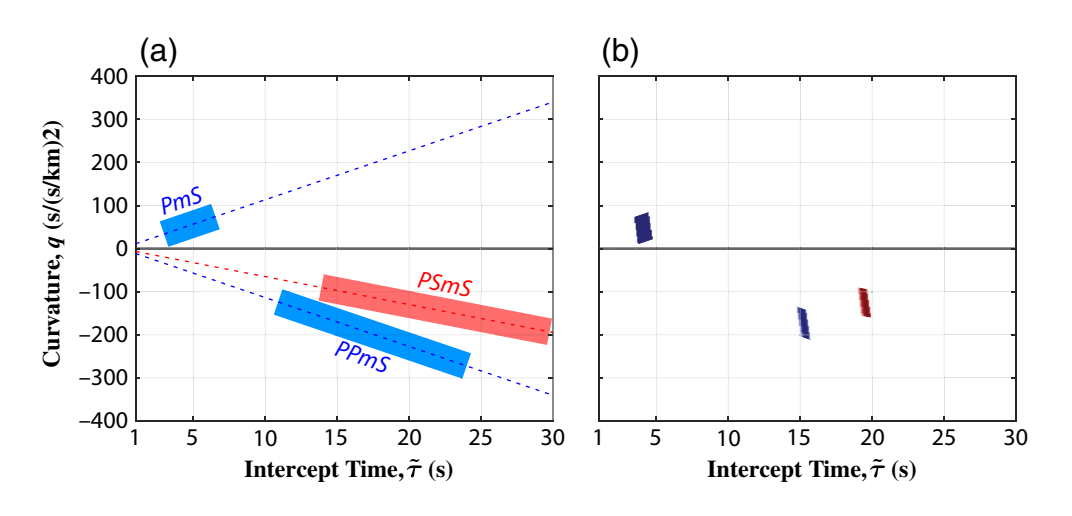


Figure 3. (a) Masking filter designed to only pass through Moho-related phases in the Radon image. Dashed lines indicate the predicted intercept-time-curvature curves for each given phase; colored rectangles indicate the final pass-through areas in the mask obtained by limiting the Moho depth and adding a tolerance width. Red and blue colors indicate positive and negative arrivals, respectively. (b) Radon image shown in Figure 2 after applying the designed crustal mask shown in panel (a). The color version of this figure is available only in the electronic edition.

H-k stacking on Radon image

The Radon image is an intercept-time-curvature domain representation of the Ps-RF data; therefore, the $H - \kappa$ stacking can also be applied to the Radon image directly before transforming it back to the time-slowness domain. In the traditional $H - \kappa$ stacking, given a pair of (H, κ) values, one can calculate the arrival times for the three phases (PmS, PPmS, and PSmS) from equation (2) and then generate a weighting trace $(\sum_i w_i G(t_i)$ in equation 1) that only has nonzero amplitudes around these arrival times. This weighting trace is then applied to all Ps-RF traces to get the stacking amplitude $s(H,\kappa)$ for this (H,κ) pair. Similarly, one can also calculate the corresponding $(\tilde{\tau}, q)$ values for the three Moho phases from equation (4b), (4d), (4f). A 2D weighting matrix can then be constructed with only nonzero elements being the 2D elliptical Gaussians centered at these three calculated $(\tilde{\tau}, q)$ locations (e.g., Fig. 5). The $H - \kappa$ stacking on the Radon image is thus conducted by a grid search of the (H, κ) pairs to maximize the stacking amplitude obtained by the element-wise product of the weighting matrix and the Radon image. This also resolves the crustal structure perfectly and shows a similar stacking image as the one applied to the time-epicentral-distance domain Ps-RF, although with a slightly larger 90% error range (33.01-36.79 km for H and 1.687–1.817 for κ ; Fig. 5b).

APPLICATION TO DATA

In this section, we apply the CRISP-RF signal denoising approach to station WCN

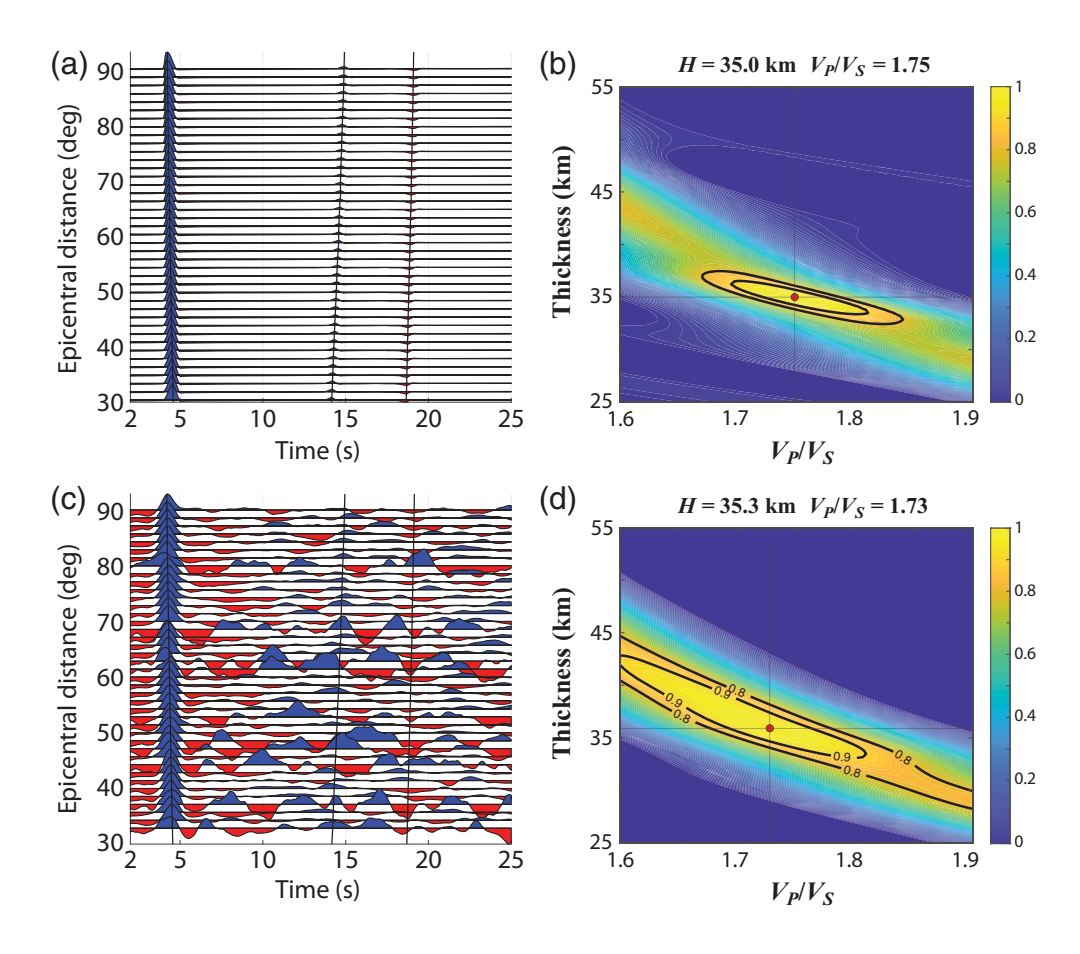


Figure 4. (a) Filtered *Ps*-RF obtained from the adjoint Radon transform of the Radon image shown in Figure 2 after applying the crustal mask shown in Figure 3. (b) $H - \kappa$ stacking of the filtered *Ps*-RF shown in panel (a). Black contour lines indicate 90% and 80% of the maximum stacking amplitude. (c,d) Raw *Ps*-RF and its $H - \kappa$ stacking for comparison; same as Figure 1b,c. The color version of this figure is available only in the electronic edition.

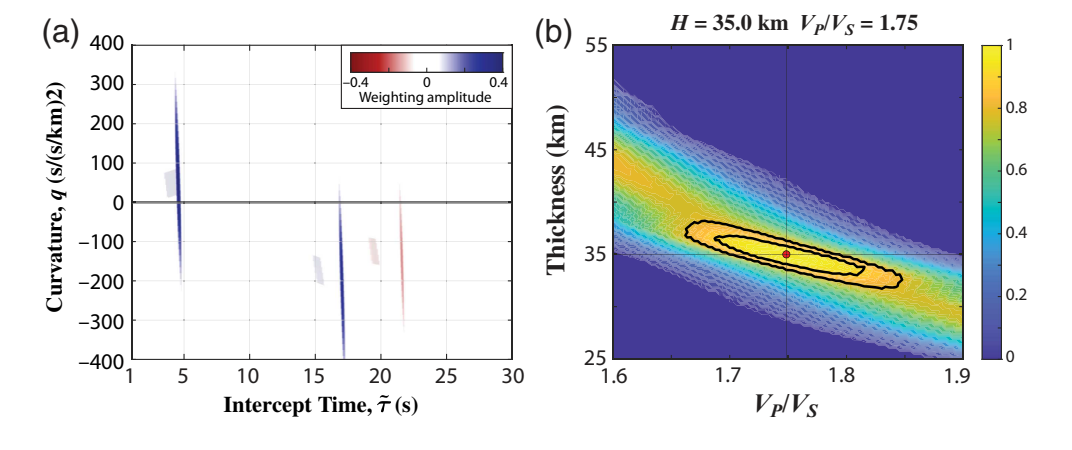
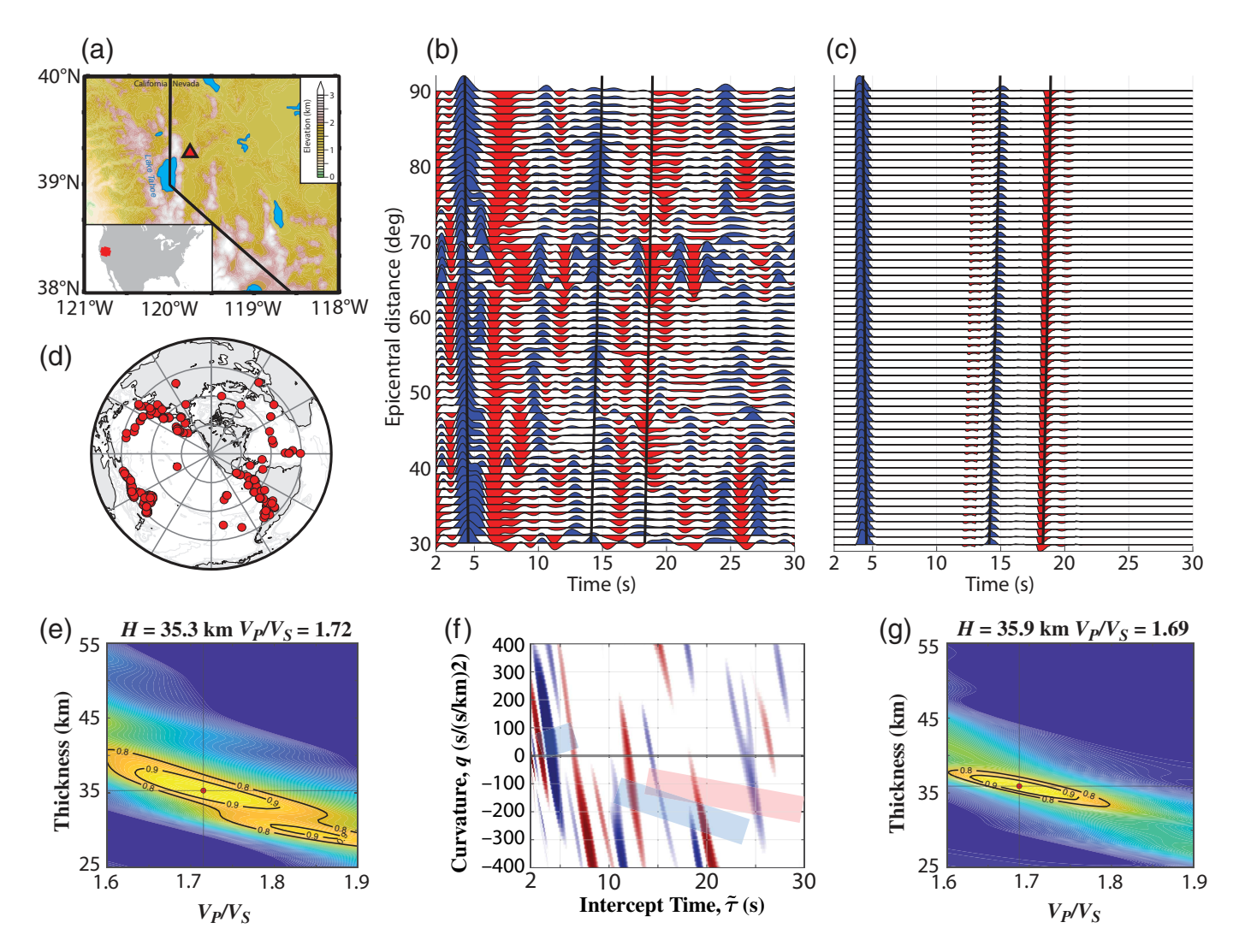


Figure 5. (a) Example of a 2D weighting matrix constructed using the searching values of H=40 km and $\kappa=1.7$. The weighting matrix is illustrated as the solid color stripes. The faded color indicates the Radon image after applying the crustal mask, same as Figure 3b. (b) $H-\kappa$ stacking of the Radon image shown in Figure 2. Black contour lines indicate 90% and 80% of the maximum stacking amplitude. The color version of this figure is available only in the electronic edition.

located in the midnorthern section of Sierra Nevada, to the northeast of Lake Tahoe (Fig. 6a). Located in the Great Valley forearc basin, this station sits on complicated crustal structures including metamorphosed ophiolites, Mesozoic-age arc-related plutons, Cenozoic-age volcanic deposits, and extensional grabens associated with sedimentation along the Basin and Range boundary (Frassetto et al., 2010). This diversity of crustal composition could likely lead to a complex teleseismic wavefield and hardto-detect Moho multiples, making it an ideal location to test the effectiveness of our approach on real seismic data.

We obtain 235 high-quality (SNR > 2.0) teleseismic events $(M_{\rm w} > 6.0,$ $30^{\circ} < \Delta < 90^{\circ}$; Fig. 6d) and calculate the Ps-RF traces using the extendedtime multi-taper approach 2000; (Park and Levin, Helffrich, 2006; Shibutani et al., 2008). We applied a cosine taper to the spectrum using a cutoff frequency of 1.0 Hz, which allows the RF to include significant information of up to \sim 0.6 Hz. We stack the Ps-RFs every 1° with 8° overlapping epicentral distance bins (Fig. 6b). We use a *P*-wave velocity of 6.3 km/s in the $H - \kappa$ stacking at this station following Wang et al. (2022). The raw Ps-RF image shows a clear direct conversion from the Moho just before 5 s and various other pulses, some of which exhibit coherence across different epicentral distances while others do not. Upon further visual inspection, a positive phase with a negative moveout can be roughly observed at around 15 s as



the *PPmS* multiple; the arrival of the *PSmS* multiple is harder to determine, as there are several negative phases between 15 and 20 s. Applying $H - \kappa$ stacking on the raw *Ps*-RF resolves a crustal thickness of 35.3 km and a *P-to-S* velocity ratio of 1.72 (Fig. 6e). This $H - \kappa$ image displays two local maxima (as defined by the 90% error range contours), indicating ambiguous stacking results due to noisy *Ps*-RF traces and poor constraints from multiple phases. For the local maxima at the optimal solution, the 90% error range is from 32.87 to 38.25 km for *H* and from 1.633 to 1.810 for κ , whereas the 80% error contour is outside the search range.

We then apply the CRISP-RF workflow on the raw Ps-RF to obtain its sparse Radon model (Fig. 6f). Although the Radon image shows more phases and is more complex compared to the synthetic one (Fig. 2) due to the complicated crustal structure detected in real seismic data, the adjoint Radon transform after applying the crustal mask gives a clean Ps-RF image with clearly identified direct conversion (PmS at \sim 5 s) and multiple reflections (PPmS at \sim 15 s and PSmS at \sim 18 s) from the Moho (Fig. 6c). Consequently, the $H-\kappa$ stacking of the filtered Ps-RF traces resolves the crustal structure with far less ambiguity, with a crustal thickness of 35.9 km and a P-to-S velocity ratio

Figure 6. (a) Location and geological settings of station WCN. Red triangle indicates the station location. The bottom-left inset map shows the location of the study area relative to the contiguous United States. (b) Raw *Ps*-RF traces calculated at station WCN plotted against epicentral distance. Black vertical lines indicate the predicted arrival times of the *PmS*, *PPmS*, and *PSmS* phases calculated from the optimal $H-\kappa$ solution. (c) Filtered *Ps*-RF traces obtained from the adjoint Radon transform of the Radon image shown in panel (f) after applying the crustal mask shown in Figure 3. (d) Location of the teleseismic events used in the RF calculation. (e) $H-\kappa$ stacking of the raw *Ps*-RF shown in panel (b). Black contour lines are 90% and 80% of the maximum stacking amplitude as indicated. (f) Sparse Radon model of the raw *Ps*-RF shown in panel (b) obtained from the CRISP-RF workflow. The crustal mask is indicated in faded color. (g) $H-\kappa$ stacking of the filtered *Ps*-RF shown in panel (c). The color version of this figure is available only in the electronic edition.

of 1.69 (Fig. 6g). This $H - \kappa$ image shows only one maxima, with the 90% error range of H and κ 40% and 29% narrower, respectively, compared to the $H - \kappa$ stacking directly on the raw Ps-RF (compare Fig. 6e and 6g; see also Table 1). The 80% error range of the $H - \kappa$ stacking on the filtered Ps-RF is from 33.17 to 38.05 km for H and from 1.610 to 1.798 for κ , which is at least 59% and 37% narrower than that on the raw Ps-RF, and is

comparable to the 90% error range of the $H - \kappa$ stacking on the raw Ps-RF. Applying the $H - \kappa$ stacking directly on the Radon image after crustal mask filtering yields a similar result (Fig. S1a, available in the supplemental material to this article). Our results are broadly consistent with Porter *et al.* (2014), which reported a Moho depth of 34.5 km and a P-to-S velocity ratio of 1.77, and the Earthscope Automated Receiver Survey (EARS, Philip Crotwell and Owens, 2005) database, which reported a crustal thickness of 38 km and a P-to-S velocity ratio of 1.70.

DISCUSSION

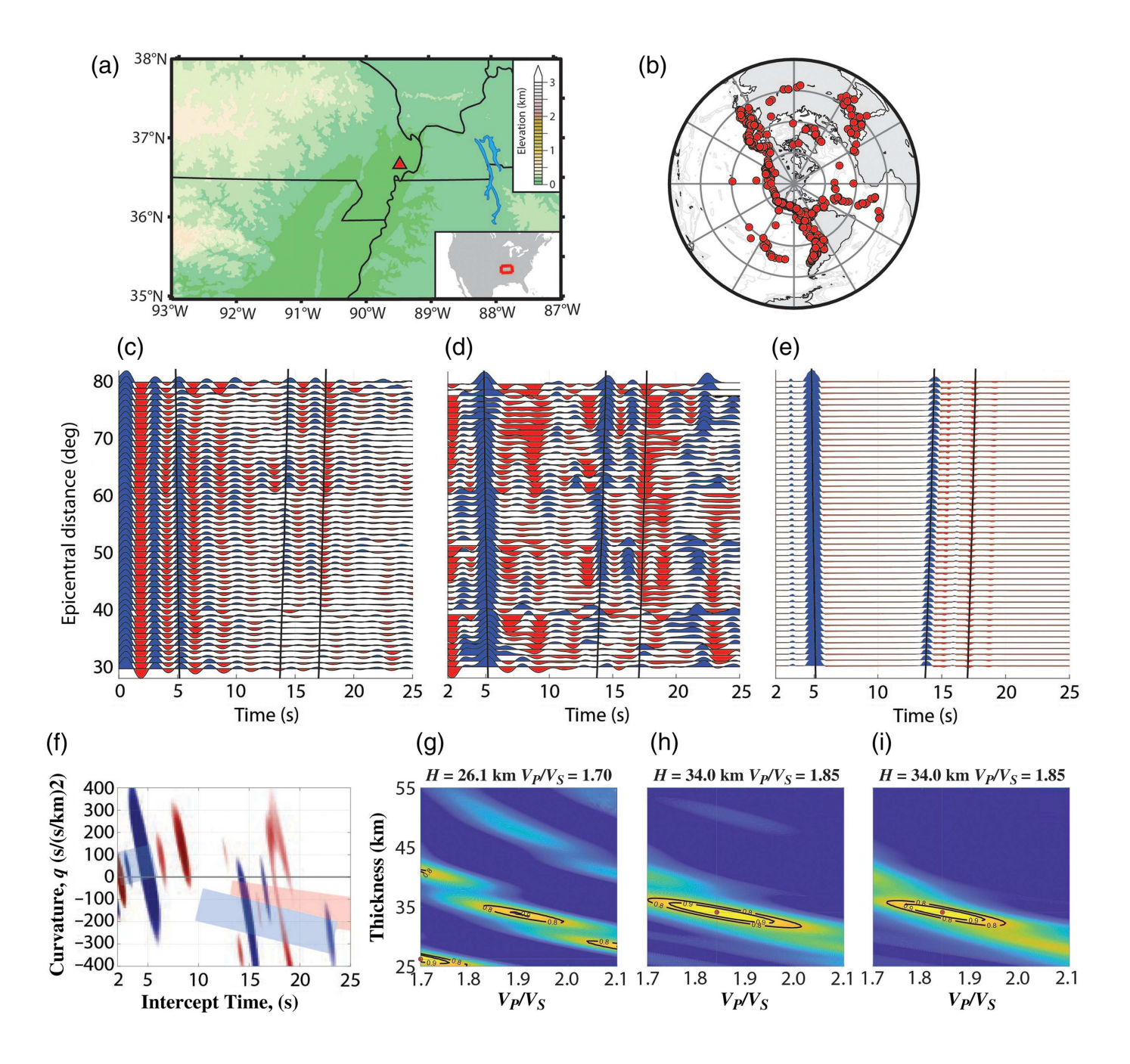
Crustal imaging through complicated structures: promises and limitations

In this study, we introduce modifications to the CRISP-RF workflow introduced by Olugboji et al. (2023) to extract Moho phases and suppress background noise using spare Radon transforms, and show that this improves the quality of crustal imaging through $H - \kappa$ stacking. Although our proposed approach is proven effective by both a synthetic experiment and a real-data example, it is based on the assumption that the Ps-RF traces are not contaminated by any significant signal-generated noise, that is, reverberations. Reverberations coming from sedimentary, oceanic, or glacial layers could generate high-amplitude resonant noise in the Ps-RF traces due to their low-seismic velocity, completely masking conversion and reflection phases from the Moho and even deeper discontinuities (Yeck et al., 2013; Yu et al., 2015; Audet, 2016; Chai et al., 2017; Cunningham and Lekic, 2019; Zhang and Gao, 2019). Because the Ps-RF traces calculated at stations above such reverberant environments are dominated by a resonance that resembles a decaying sinusoid, the proposed approach in this study will likely fail because the distinct, time-separated, and coherent arrivals are no longer present. A systematic datadriven approach—FAst Detection and Elimination of Echoes and Reverberations (FADER)—has recently been proposed by Zhang and Olugboji (2023) to solve the twin problem of detection and elimination of reverberations without a priori knowledge of the elastic structure of the reverberant layers. This approach uses autocorrelation and cepstral analysis to extract the signature of reverberation and then uses a frequency domain filter to remove it and obtain reverberation-free Ps-RF. Therefore, it is natural to combine both the techniques to achieve a better crustal image in reverberant settings.

To demonstrate the possibility of applying our proposed approach after filtering out reverberation, we select station HENM located in the Upper Mississippi embayment, where loose sediments are widely present (Fig. 7a). We obtain 192 high-quality (SNR > 2.0) teleseismic events ($M_{\rm w} > 6.0$, $30^{\rm o} < \Delta < 90^{\rm o}$; Fig. 7b) and calculate the *Ps*-RF traces using the same method and parameters described earlier. We use a *P*-wave velocity of 6.1 km/s in the $H-\kappa$ stacking at this station following Liu *et al.* (2017). The raw *Ps*-RF traces show strong reverberant behavior with no clearly identified phases

(Fig. 7c) and therefore lead to a poorly constrained $H - \kappa$ stacking image with multiple local maxima and an optimal stacking solution at the boundary of the search range (Fig. 7g). We apply the FADER workflow and estimate a two-way travel time (of the S waveleg trapped in the sediment layer) of 1.18 s and a reverberation strength (at the sediment-crust boundary) of 0.70 (see Fig. S2). A frequency domain resonance removal filter is then designed and applied to the raw Ps-RF traces, which effectively eliminates the resonant noise, making the direct conversion from the Moho clearly visible at around 5 s, along with the two multiple phases at around 14 s and 17 s, respectively, although not as coherent (Fig. 7d). This results in a much better constrained $H - \kappa$ stacking image, with an optimal solution of 34.0 km for H and 1.85 for κ (Fig. 7h; see Table 1 for the 90% error range). Applying the proposed approach in this study further eliminates all phases and background noise except for the Moho phases, resulting in a clean, noise-free Ps-RF image (Fig. 7e). The consequent $H - \kappa$ stacking gives the same solution of H = 34.0 km and $\kappa = 1.85$, with an even narrow 90% error range (38% narrower for H and 42% narrower for κ) (compare Fig. 7h and 7i; see also Table 1). Applying the $H - \kappa$ stacking directly on the Radon image after crustal mask filtering yields a similar result (Fig. S1b). This result differs from those documented in the EARS database (H = 28 km, $\kappa = 1.76$) due to the extra processing step of FADER but is consistent with Liu et al. (2017), which implemented a similar reverberation removal technique and reported a Moho depth of 34.1 km and a P-to-S velocity ratio of 1.85.

The shallow layer reverberations commonly observed in geological settings such as sediments, oceans, and glaciers are a special complicating case where near-surface crustal structure hampers the reliability of Ps-RF imaging results. Other cases include a crust-to-mantle transition that is gradational or a complex crustal structure, for example, dipping Moho, intracrustal layers, and crustal anisotropy (Frederiksen and Bostock, 2000; Ogden et al., 2019; Shi et al., 2023). In these cases, the crustal properties deviate from the simple case considered in our synthetic experiments (a single layer with a sharp Moho). For instance, in the data example of station WCN we showed earlier, a strong negative phase with a negative moveout can be observed at ~7 s in the raw Ps-RF traces (Fig. 6b) and also in the negative curvature domain of the Radon image (Fig. 6f). This phase is likely a multiple reflection generated at a shallow interface within the crust. In addition, complicated phases with alternate positive and negative amplitudes are observed at ~10-12 s (Fig. 6b), possibly indicating the presence of upper mantle anisotropy. In this case, a joint interpretation of radial and transverse RFs may aid in identifying complex structural features. Although we have demonstrated that our data processing workflow can robustly recover the bulk crust properties, we recommend caution when applying our proposed approach under these circumstances due to the difficulty of interpreting a possibly more complicated Radon image.



Improving constraints on crustal composition and evolution

P-to-S velocity ratio (κ) can be directly converted to Poisson's ratio (σ) (Christensen and Fountain, 1975):

$$\sigma = 0.5 \left[1 - \frac{1}{\kappa^2 - 1} \right]. \tag{5}$$

Improved resolution of κ following denoising provides much tighter constraints on the inferred crustal composition, providing important information on the geological evolution of the Earth's crust (Zandt and Ammon, 1995; Stankiewicz *et al.*, 2002; Guo *et al.*, 2019). For instance, an increase in plagioclase content and a decrease in quartz can increase the

Figure 7. (a) Location and geological settings of station HENM. Red triangle indicates the station location. The bottom-right inset map shows the location of the study area relative to the contiguous United States. (b) Location of the teleseismic events used in the RF calculation. (c) Raw *Ps*-RF traces calculated at station HENM plotted against epicentral distance. Theoretical arrival times of *PmS*, *PPmS*, and *PSmS* phases are calculated from the $H-\kappa$ stacking result and plotted in solid black lines. (d) *Ps*-RF traces after reverberation removal. (e) *Ps*-RF traces after reverberation removal and applying the modified CRISP-RF workflow. (f) Sparse Radon model of the raw *Ps*-RF shown in panel (d) obtained from the CRISP-RF workflow. The crustal mask is indicated in faded color. (g) $H-\kappa$ stacking of the raw Ps-RF shown in panel (c). (h) $H-\kappa$ stacking of the processed *Ps*-RF shown in panel (d). (i) $H-\kappa$ stacking of the processed *Ps*-RF shown in panel (e). The color version of this figure is available only in the electronic edition.

Poisson's ratio from 0.24 for a granitic rock to 0.27 for a diorite and to 0.30 for a gabbro (Tarkov and Vavakin, 1982).

RF imaging studies have routinely used this sensitivity of crustal composition to Poisson's ratio to study how bulk composition varies for different geological terranes. For example, thanks to the massive high-quality seismic data from USArray and EARS (Philip Crotwell and Owens, 2005), Lowry and Pérez-Gussinyé (2011) proposed a feedback mechanism for which ductile strain first localizes quartz-rich, weak crust, leading to processes that promote advective warming, hydration, and further weakening, based on the correlation between low Poisson's ratios, higher lithospheric temperatures, and deformation in the Cordillera region. Similarly, Ma and Lowry (2017) estimated the seismic velocity ratios across the continent United States and suggested Cordilleran high heat flow may partly reflect crustal hydration enthalpy. Other examples include Audet et al. (2009), which implied high pore-fluid pressures and thus an overpressured subducted oceanic crust at northern Cascadia indicated by anomalously high Poisson's ratio and He et al. (2013), which suggested a dominantly felsic lower crust and the presence of lower crustal delamination in the Cathaysia block in Southern China from the low Poisson's ratio.

The reliability of these interpretations depends heavily on the accuracy of the *P-to-S* velocity ratio (κ) estimation. We have shown that by denoising the *Ps*-RF using our proposed approach, the measurement error for κ in the traditional $H - \kappa$ stacking can be greatly reduced (Table 1), enabling more robust estimation of crustal structures.

Application of Radon transform in seismic signal processing

We have applied a sparse Radon transform in high-resolution Ps-RF imaging of sharp discontinuities. Because we have demonstrated earlier, this data processing technique can be beneficial not only when imaging upper mantle discontinuities, as suggested by Olugboji et al. (2023), but also for improved detection of multiple reflected phases when imaging the crust. The Radon transform maps the coherent phases in the time-domain Ps-RF traces onto the Radon model based on their moveout and amplitudes. The same philosophy is also applicable to other seismic imaging techniques, for example, top- and bottom-side reflections, because each arriving phase also follows a distinct moveout (Gu et al., 2009; Gu and Sacchi, 2009). In these cases, modifications to equations (2)-(4) are needed, as the theoretical arrivals in these observations are different, and their relationship with slowness or epicentral distance may be different (e.g., linear instead of parabolic).

CONCLUSION

In this study, we use a sparsity-promoting Radon transform to decompose the *Ps*-RF into its scattered wave contributions, that is, direct conversions, multiples, and incoherent noise.

By applying a specially designed crustal mask to the Radon model and transforming the now filtered Ps-RFs into the time domain using an adjoint Radon transform, a set of clean, noisefree Ps-RF traces is obtained. This leads to robust interpretations of crustal structure. This technique for crustal imaging using Ps-RFs is a modification to the CRISP-RF workflow proposed by Olugboji et al. (2023), which originally targets upper mantle discontinuities. We demonstrate using both synthetic experiments and real-data examples that our approach can effectively denoise the Ps-RF traces and extract all Moho phases, and therefore greatly reduce the error range in the grid search for crustal parameters. We also demonstrate the CRISP-RF denoising with a simultaneous dereverberation technique proposed by Zhang and Olugboji (2021, 2023), which improves crustal imaging beneath reverberant layers. In the presence of complex crustal structures, for example, dipping Moho, intracrustal layers, and crustal anisotropy, we recommend caution when applying our proposed approach due to the difficulty of interpreting a possibly more complicated Radon image. We anticipate that our approach will enable high-resolution crustal imaging with noisy teleseismic RFs and inspire more applications of the sparse Radon transform for seismic imaging.

DATA AND RESOURCES

All seismic data used in this study can be obtained from the Incorporated Research Institutions for Seismology Data Management Center (IRIS-DMC, https://ds.iris.edu/ds, last accessed December 2023) under the network codes NN (station WCN) and NM (station HENM). Synthetic receiver functions (RFs) were computed using the Telewavesim open-source Python library provided by Audet et al. (2019). The extended-time multitaper deconvolution program and the Clean Receiver Function Imaging using SParse Radon Filter (CRISP-RF) data processing workflow are provided by Olugboji et al. (2023), and can be retrieved from the open-source repository at doi: 10.5281/zenodo.7996504. The FAst Detection and Elimination of Echoes and Reverberations (FADER) data processing workflow is provided by Zhang and Olugboji (2023) and can be retrieved from the open-source repository at doi: 10.5281/zenodo. 6804873. The supplemental material includes Figure S1 of $H-\kappa$ stacking on Radon images for real data examples and Figure S2 of reverberation detection with FADER at station HENM.

DECLARATION OF COMPETING INTERESTS

The authors acknowledge that there are no conflicts of interest recorded.

ACKNOWLEDGMENTS

This work was made possible by the support from the National Science Foundation (NSF) under Grant Number 1818654. The authors acknowledge the use of the BlueHive Linux cluster at the University of Rochester's Center for Integrated Research Computing (CIRC, https://www.circ.rochester.edu/, last accessed December 2023). The authors thank Vadim Levin and one anonymous reviewer whose comments significantly improved the article.

REFERENCES

- Akuhara, T., K. Mochizuki, H. Kawakatsu, and N. Takeuchi (2016). Non-linear waveform analysis for water-layer response and its application to high-frequency receiver function analysis using OBS array, Geophys. J. Int. 206, no. 3, 1914–1920, doi: 10.1093/gji/ggw253.
- Ammon, C. J. (1991). The isolation of receiver effects from teleseismic P waveforms, *Bull. Seismol. Soc. Am.* **81**, no. 6, 2504–2510.
- Audet, P. (2016). Receiver functions using OBS data: promises and limitations from numerical modelling and examples from the cascadia initiative, *Geophys. J. Int.* **205**, no. 3, 1740–1755, doi: 10.1093/gji/ggw111.
- Audet, P., M. G. Bostock, N. I. Christensen, and S. M. Peacock (2009). Seismic evidence for overpressured subducted oceanic crust and megathrust fault sealing, *Nature* 457, no. 7225, 76–78, doi: 10.1038/nature07650.
- Audet, P., C. Thomson, M. Bostock, and T. Eulenfeld (2019). Telewavesim: Python software for teleseismic body wave modeling, J. Open Source Softw. 4, no. 44, 1818, doi: 10.21105/joss.01818.
- Bodin, T., H. Yuan, and B. Romanowicz (2013). Inversion of receiver functions without deconvolution—Application to the Indian craton, *Geophys. J. Int.* **196**, no. 2, 1025–1033, doi: 10.1093/gji/ggt431.
- Chai, C., C. J. Ammon, S. Anandakrishnan, C. Ramirez, and A. Nyblade (2017). Estimating subglacial structure using p-wave receiver functions, *Geophys. J. Int.* 209, no. 2, 1064–1079, doi: 10.1093/gji/ggx075.
- Chen, K.-X., K. M. Fischer, J. Hua, and Y. Gung (2020). Imaging crustal melt beneath northeast japan with ps receiver functions, *Earth Planet. Sci. Lett.* **537**, 116173, doi: 10.1016/j.epsl.2020.116173.
- Chen, Y., J. Chen, B. Guo, S. Qi, and P. Zhao (2019). Denoising the receiver function through curvelet transforming and migration imaging, *Chin. J. Geophys.* **62**, no. 6, 2027–2037.
- Chen, Y., Y. J. Gu, Q. Zhang, H. Wang, P. Zuo, and Y. Chen (2022). Leastsquares migration imaging of receiver functions, doi: 10.1002/essoar.10512413.1.
- Christensen, N. I., and D. M. Fountain (1975). Constitution of the lower continental crust based on experimental studies of seismic velocities in granulite, *GSA Bull.* **86**, no. 2, 227–236.
- Cunningham, E., and V. Lekic (2019). Constraining crustal structure in the presence of sediment: A multiple converted wave approach, *Geophys. J. Int.* **219**, no. 1, 313–327, doi: 10.1093/gji/ggz298.
- Dalai, B., P. Kumar, and X. Yuan (2019). De-noising receiver function data using the seislet transform, *Geophys. J. Int.* **217**, no. 3, 2047–2055, doi: 10.1093/gji/ggz135.
- Dalai, B., P. Kumar, U. Srinu, and M. K. Sen (2021). De-noising receiver function data using the unsupervised deep learning approach, *Geophys. J. Int.* **229**, no. 2, 737–749, doi: 10.1093/gji/ggab494.
- Dokht, R. M. H., Y. J. Gu, and M. D. Sacchi (2016). Singular spectrum analysis and its applications in mapping mantle seismic structure, *Geophys. J. Int.* **208**, no. 3, 1430–1442, doi: 10.1093/gji/ggw473.
- Eaton, D. W., S. Dineva, and R. Mereu (2006). Crustal thickness and VP/VS variations in the Grenville orogen (Ontario, Canada) from analysis of teleseismic receiver functions, *Tectonophysics* **420**, no. 1, 223–238, doi: 10.1016/j.tecto.2006.01.023.
- Frassetto, A., G. Zandt, H. Gilbert, T. J. Owens, and C. H. Jones (2010). Improved imaging with phase-weighted common conversion point stacks of receiver functions, *Geophys. J. Int.* **182**, no. 1, 368–374, doi: 10.1111/j.1365-246X.2010.04617.x.

- Frederiksen, A. W., and M. G. Bostock (2000). Modelling teleseismic waves in dipping anisotropic structures, *Geophys. J. Int.* **141**, no. 2, 401–412, doi: 10.1046/j.1365-246x.2000.00090.x.
- Gong, C., L. Chen, Z. Xiao, and X. Wang (2022). Deep learning for quality control of receiver functions, *Front. Earth Sci.* **10**, 921830, doi: 10.3389/feart.2022.921830.
- Gu, Y. J., and M. Sacchi (2009). Radon transform methods and their applications in mapping mantle reflectivity structure, *Surv. Geophys.* 30, no. 4, 327–354, doi: 10.1007/s10712-009-9076-0.
- Gu, Y. J., Y. An, M. Sacchi, R. Schultz, and J. Ritsema (2009). Mantle reflectivity structure beneath oceanic hotspots, *Geophys. J. Int.* **178**, no. 3, 1456–1472.
- Guo, L., R. Gao, L. Shi, Z. Huang, and Y. Ma (2019). Crustal thickness and poisson's ratios of south china revealed from joint inversion of receiver function and gravity data, *Earth Planet. Sci. Lett.* 510, 142–152, doi: 10.1016/j.epsl.2018.12.039.
- Gurrola, H., G. E. Baker, and J. B. Minster (1995). Simultaneous time-domain deconvolution with application to the computation of receiver functions, *Geophys. J. Int.* **120**, no. 3, 537–543, doi: 10.1111/j.1365-246X.1995.tb01837.x.
- He, C., S. Dong, M. Santosh, and X. Chen (2013). Seismic evidence for a geosuture between the yangtze and cathaysia blocks, South China, *Sci. Rep.* **3,** 2200, doi: 10.1038/srep02200.
- Helffrich, G. (2006). Extended-time multitaper frequency domain cross correlation receiver-function estimation, *Bull. Seismol. Soc. Am.* **96**, no. 1, 344–347, doi: 10.1785/0120050098.
- Helffrich, G., and D. Thompson (2010). A stacking approach to estimate VP/VS from receiver functions: Stacking to estimate VP/VS, *Geophys. J. Int.* **182**, no. 2, 899–902, doi: 10.1111/j.1365-246X.2010.04628.x.
- Julia, J., C. J. Ammon, R. B. Herrmann, and A. M. Correig (2000). Joint inversion of receiver function and surface wave dispersion observations, *Geophys. J. Int.* 143, no. 1, 99–112.
- Kim, D., V. Lekić, J. C. E. Irving, N. Schmerr, B. Knapmeyer-Endrun, R. Joshi, M. P. Panning, B. Tauzin, F. Karakostas, R. Maguire, *et al.* (2021). Improving constraints on planetary interiors with PPs receiver functions, *J. Geophys. Res.* **126**, no. 11, e2021JE006983, doi: 10.1029/2021JE006983.
- Kim, H., H. Kawakatsu, T. Akuhara, M. Shinohara, H. Shiobara, H. Sugioka, and R. Takagi (2021). Receiver function imaging of the amphibious NE japan subduction zone—Effects of low-velocity sediment layer, *J. Geophys. Res.* 126, no. 9, e2021JB021918, doi: 10.1029/2021jb021918.
- Krueger, H. E., I. Gama, and K. M. Fischer (2021). Global patterns in cratonic mid-lithospheric discontinuities from sp receiver functions, *Geochem. Geophys. Geosys.* **22**, no. 6, e2021GC009819, doi: 10.1029/2021gc009819.
- Kumar, M. R., and M. G. Bostock (2008). Extraction of absolute P velocity from receiver functions, *Geophys. J. Int.* **175,** no. 2, 515–519, doi: 10.1111/j.1365-246X.2008.03963.x.
- Langston, C. A. (1979). Structure under Mount Rainier, Washington, inferred from tele-seismic body waves, *J. Geophys. Res.* **84**, no. B9, 4749, doi: 10.1029/JB084iB09p04749.
- Leahy, G. M., J. A. Collins, C. J. Wolfe, G. Laske, and S. C. Solomon (2010). Underplating of the hawaiian swell: Evidence from teleseismic receiver functions, *Geophys. J. Int.* **183**, no. 1, 313–329, doi: 10.1111/j.1365-246X.2010.04720.x.

- Ligorría, J. P., and C. J. Ammon (1999). Iterative deconvolution and receiverfunction estimation, *Bull. Seismol. Soc. Am.* 89, no. 5, 1395–1400, doi: 10.1785/BSSA0890051395.
- Liu, L., S. S. Gao, K. H. Liu, and K. Mickus (2017). Receiver function and gravity constraints on crustal structure and vertical movements of the upper Mississippi embayment and Ozark uplift, J. Geophys. Res. 122, no. 6, 4572–4583, doi: 10.1002/2017jb014201.
- Lognonné, P., W. B. Banerdt, W. T. Pike, D. Giardini, U. Christensen, R. F. Garcia, T. Kawamura, S. Kedar, B. Knapmeyer-Endrun, L. Margerin, et al. (2020). Constraints on the shallow elastic and anelastic structure of mars from InSight seismic data, *Nature Geosci.* 13, no. 3, 213–220, doi: 10.1038/s41561-020-0536-y.
- Lowry, A. R., and M. Pérez-Gussinyé (2011). The role of crustal quartz in controlling cordilleran deformation, *Nature* **471**, no. 7338, 353–357, doi: 10.1038/nature09912.
- Ma, X., and A. R. Lowry (2017). USArray imaging of continental crust in the conterminous United States, *Tectonics* **36**, no. 12, 2882–2902, doi: 10.1002/2017TC004540.
- Ogden, C. S., I. D. Bastow, A. Gilligan, and S. Rondenay (2019). A reappraisal of the $H-\kappa$ stacking technique: Implications for global crustal structure, *Geophys. J. Int.* **219**, no. 3, 1491–1513, doi: 10.1093/gji/ggz364.
- Olugboji, T., J. Park, S.-I. Karato, and M. Shinohara (2016). Nature of the seismic lithosphere-asthenosphere boundary within normal oceanic mantle from high-resolution receiver functions, *Geochem. Geophys. Geosys.* 17, no. 4, 1265–1282, doi: 10.1002/2015GC006214.
- Olugboji, T., Z. Zhang, S. Carr, C. Ekmekci, and M. Cetin (2023). On the detection of upper mantle discontinuities with radon-transformed PS receiver functions (CRISP-RF), *Geophys. J. Int.* **236**, no. 2, 748–763, doi: 10.1093/gji/ggad447.
- Park, J., and V. Levin (2000). Receiver functions from multiple-taper spectral correlation estimates, *Bul. Seismol. Soc. Am.* **90**, no. 6, 1507–1520, doi: 10.1785/0119990122.
- Park, J., and V. Levin (2016). Anisotropic shear zones revealed by backazimuthal harmonics of teleseismic receiver functions, *Geophys. J. Int.* **207**, no. 2, 1216–1243, doi: 10.1093/gji/ggw323.
- Parker, E. H., R. B. Hawman Jr., K. M. Fischer, and L. S. Wagner (2013). Crustal evolution across the Southern Appalachians: Initial results from the SESAME broadband array, *Geophys. Res. Lett.* 40, no. 15, 3853–3857, doi: 10.1002/grl.50761.
- Philip Crotwell, H., and T. J. Owens (2005). Automated receiver function processing, *Seismol. Res. Lett.* **76**, no. 6, 702–709, doi: 10.1785/gssrl.76.6.702.
- Porter, R. C., M. J. Fouch, and N. C. Schmerr (2014). Dynamic lithosphere within the great basin, *Geochem. Geophys. Geosys.* **15**, no. 4, 1128–1146, doi: 10.1002/2013GC005151.
- Rivadeneyra-Vera, C., M. Bianchi, M. Assumpção, V. Cedraz, J. Julià, M. Rodríguez, L. Sánchez, G. Sánchez, L. Lopez-Murua, G. Fernandez, et al. (2019). An updated crustal thickness map of central South America based on receiver function measurements in the region of the Chaco, Pantanal, and Paraná basins, southwestern Brazil, J. Geophys. Res. 124, no. 8, 8491–8505, doi: 10.1029/2018jb016811.
- Rondenay, S. (2009). Upper mantle imaging with array recordings of converted and scattered teleseismic waves, *Surv. Geophys.* **30**, no. 4, 377–405, doi: 10.1007/s10712-009-9071-5.
- Rubio, G., Y. Chen, M. D. Sacchi, and Y. J. Gu (2020). 3-D and 5-D reconstruction of P receiver functions via multichannel singular

- spectrum analysis, *Geophys. J. Int.* **225**, no. 2, 1110–1128, doi: 10.1093/gji/ggaa541.
- Ryberg, T., and M. Weber (2000). Receiver function arrays: A reflection seismic approach, *Geophys. J. Int.* **141,** no. 1, 1–11, doi: 10.1046/j.1365-246X.2000.00077.x.
- Rychert, C. A., and N. Harmon (2016). Stacked P-to-S and S-to-P receiver functions determination of crustal thickness, vp, and vs: The H-V stacking method, *Geophys. Res. Lett.* **43**, no. 4, 1487–1494.
- Rychert, C. A., N. Harmon, and S. Tharimena (2018). Scattered wave imaging of the oceanic plate in Cascadia, *Sci. Adv.* **4,** no. 2, eaao1908, doi: 10.1126/sciadv.aao1908.
- Rychert, C. A., G. Laske, N. Harmon, and P. M. Shearer (2013). Seismic imaging of melt in a displaced hawaiian plume, *Nature Geosci.* **6**, no. 8, 657–660, doi: 10.1038/ngeo1878.
- Shi, J., T. Wang, and L. Chen (2020). Receiver function velocity analysis technique and its application to remove multiples, *J. Geophys. Res.* **125**, no. 8, B11309, doi: 10.1029/2020JB019420.
- Shi, Y., Y. Gao, H. Zhang, Z. Zhang, and G. Li (2023). Crustal azimuthal anisotropy in the lateral collision zone of the SE margin of the Tibetan plateau and its tectonic implications, *Geophys. J. Int.* **234**, no. 1, 1–11, doi: 10.1093/gji/ggad059.
- Shibutani, T., T. Ueno, and K. Hirahara (2008). Improvement in the extended-time multitaper receiver function estimation technique, *Bull. Seismol. Soc. Am.* **98**, no. 2, 812–816, doi: 10.1785/0120070226.
- Stankiewicz, J., S. Chevrot, R. D. van der Hilst, and M. J. de Wit (2002). Crustal thickness, discontinuity depth, and upper mantle structure beneath southern Africa: Constraints from body wave conversions, *Phys. Earth Planet. In.* **130**, no. 3, 235–251, doi: 10.1016/S0031-9201(02)00012-2.
- Tarkov, A. P., and V. V. Vavakin (1982). Poisson's ratio behaviour in various crystalline rocks: Application to the study of the earth's interior, *Phys. Earth Planet. In.* **29**, no. 1, 24–29, doi: 10.1016/0031-9201(82)90134-0.
- Thompson, D. A., I. D. Bastow, G. Helffrich, J.-M. Kendall, J. Wookey, D. B. Snyder, and D. W. Eaton (2010). Precambrian crustal evolution: Seismic constraints from the canadian shield, *Earth Planet*. *Sci. Lett.* **297**, no. 3, 655–666, doi: 10.1016/j.epsl.2010.07.021.
- Vanacore, E. A., T. Taymaz, and E. Saygin (2013). Moho structure of the anatolian plate from receiver function analysis, *Geophys. J. Int.* **193**, no. 1, 329–337, doi: 10.1093/gji/ggs107.
- Wang, F., X. Song, and J. Li (2022). Deep learning-based *H* κmethod (HkNet) for estimating crustal thickness and *VP/VS* ratio from receiver functions, *J. Geophys. Res.* **127**, no. 6, e2022JB023944, doi: 10.1029/2022jb023944.
- Wang, K., S. Wu, and P. Tong (2022). Crustal deformation in the Sierra Nevada and Walker Lane region inferred from P-wave azimuthal anisotropy, *J. Geophys. Res.* **127**, no. 12, e2022JB024554, doi: 10.1029/2022JB024554.
- Wittlinger, G., V. Farra, G. Hetényi, J. Vergne, and J. Nábělek (2009). Seismic velocities in southern Tibet lower crust: A receiver function approach for eclogite detection, *Geophys. J. Int.* 177, no. 3, 1037–1049, doi: 10.1111/j.1365-246X.2008.04084.x.
- Xia, B., H. Thybo, and I. M. Artemieva (2017). Seismic crustal structure of the North China craton and surrounding area: Synthesis and analysis, *J. Geophys. Res.* **122**, no. 7, 5181–5207, doi: 10.1002/2016jb013848.

- Yang, X., G. L. Pavlis, M. W. Hamburger, S. Marshak, H. Gilbert, J. Rupp, T. H. Larson, C. Chen, and N. S. Carpenter (2017). Detailed crustal thickness variations beneath the Illinois basin area: Implications for crustal evolution of the midcontinent, *J. Geophys. Res.* 122, no. 8, 6323–6345, doi: 10.1002/2017jb014150.
- Yang, X., G. L. Pavlis, and Y. Wang (2016). A quality control method for teleseismic P-wave receiver functions, *Bull. Seismol. Soc. Am.* 106, no. 5, 1948–1962, doi: 10.1785/0120150347.
- Yeck, W. L., A. F. Sheehan, and V. Schulte-Pelkum (2013). Sequential Hstacking to obtain accurate crustal thicknesses beneath sedimentary basins, *Bull. Seismol. Soc. Am.* 103, no. 3, doi: 10.1785/0120120290.
- Yu, Y., J. Song, K. H. Liu, and S. S. Gao (2015). Determining crustal structure beneath seismic stations overlying a low-velocity sedimentary layer using receiver functions, *J. Geophys. Res.* 120, no. 5, 3208–3218, doi: 10.1002/2014JB011610.
- Yuan, H. (2015). Secular change in archaean crust formation recorded in western Australia, *Nature Geosci.* 8, no. 10, 808–813, doi: 10.1038/ngeo2521.
- Zandt, G., and C. J. Ammon (1995). Continental crust composition constrained by measurements of crustal poisson's ratio, *Nature* **374**, no. 6518, 152–154, doi: 10.1038/374152a0.
- Zhang, Z., and Y. Gao (2019). Crustal thicknesses and poisson's ratios beneath the Chuxiong-Simao basin in the southeast margin of the tibetan plateau, *Earth Planet. Phys.* **3**, no. 1, 69–84.

- Zhang, Z., and T. Olugboji (2021). The signature and elimination of sediment rever-berations on submarine receiver functions, *J. Geophys. Res.* **126**, no. 5, e2020JB021567, doi: 10.1029/2020jb021567.
- Zhang, Z., and T. Olugboji (2023). Lithospheric imaging through reverberant layers: Sediments, oceans, and glaciers, *J. Geophys. Res.* **128**, no. 5, e2022JB026348, doi: 10.1029/2022jb026348.
- Zhang, Q., Y. Chen, F. Zhang, and Y. Chen (2022). Improving receiver function imaging with high-resolution radon transform, *Geophys. J. Int.* **230**, no. 2, 1292–1304, doi: 10.1093/gji/ggac116.
- Zhang, Q., H. Wang, W. Chen, and G. Huang (2021). A robust method for random noise suppression based on the radon transform, *J. Appl. Geophys.* **184**, 104183, doi: 10.1016/j.japp-geo.2020.104183.
- Zhong, M., and Z. Zhan (2020). An array-based receiver function deconvolution method: Methodology and application, *Geophys. J. Int.* **222**, no. 1, 1–14, doi: 10.1093/gji/ggaa113.
- Zhu, L., and H. Kanamori (2000). Moho depth variation in southern California from teleseismic receiver functions, *J. Geophys. Res.* **105**, no. B2, 2969–2980, doi: 10.1029/1999JB900322.

Manuscript received 11 October 2023 Published online 8 January 2024